
Article:
Franco Cairo, João Paulo L. orcid.org/0000-0002-4744-3111, Almeida, Dnane V., Andrade, Viviane B. et al. (10 more authors) (2024) Biochemical and structural insights of a recombinant AA16 LPMO from the marine and sponge-symbiont Peniophora sp. International journal of biological macromolecules. 135596. ISSN 0141-8130

https://doi.org/10.1016/j.ijbiomac.2024.135596

Biochemical and structural insights of a recombinant AA16 LPMO from the marine and sponge-symbiont *Peniophora* sp

João Paulo L. Franco Cairo[a,b,c], Dnane V. Almeida[d], Viviane B. Andrade[d], César R. F. Terrasan[b], Abbey Telfer[c], Thiago A. Gonçalves[a], Daniel E. Diaz[c], Fernanda L. Figueiredo[b], Livia B. Brenelli[b], Paul H. Walton[c], André Damasio[b], Wanius Garcia[d], Fabio M. Squina[a*]

[a] Programa de Processos Tecnológicos e Ambientais, Universidade de Sorocaba (UNISO), Sorocaba, Brazil
[b] Laboratory of Enzymology and Molecular Biology of Microorganisms (LEBIMO), Department of Biochemistry and Tissue Biology, Institute of Biology, State University of Campinas (UNICAMP), Campinas, São Paulo, Brazil
[c] Department of Chemistry, University of York, York, United Kingdom
[d] Centro de Ciências Naturais e Humanas (CCNH), Universidade Federal do ABC (UFABC), Santo André, SP, Brazil

Abstract

Lytic polysaccharide monooxygenases (LPMOs) are copper-dependent enzymes that oxidize polysaccharides, leading to their cleavage. LPMOs are classified into eight CAZY families (AA9-11, AA13-17), with the functionality of AA16 being poorly characterized. This study presents biochemical and structural data for an AA16 LPMO (*Pn*AA16) from the marine sponge symbiont *Peniophora* sp. Phylogenetic analysis revealed that *Pn*AA16 clusters separately from previously characterized AA16s. However, the structural modelling of *Pn*AA16 showed the characteristic immunoglobulin-like fold of LPMOs, with a conserved his-brace motif coordinating a copper ion. The copper-bound *Pn*AA16 showed greater thermal stability than its apo-form, highlighting copper's role in enzyme stability. Functionally, *Pn*AA16 demonstrated oxidase activity, producing 5 μM H_2O_2 after 30 minutes, but showed 20 times lower peroxidase activity (0.27 U/g) compared to a fungal AA9. Specific activity assays indicated that *Pn*AA16 acts only on cellohexaose, generating native celloligosaccharides (C3 to C5) and oxidized products with regioselective oxidation at C1 and C4 positions. Finally, *Pn*AA16 boosted the activity of a cellulolytic cocktail for cellulose saccharification in the presence of ascorbic acid, hydrogen peroxide, or both. In conclusion, the present work provides insights into the AA16 family, expanding the understanding of their structural and functional relationships and biotechnological potential.

Keywords: LPMOs, AA16, *Peniophora*

Introduction

(Lytic) polysaccharide monooxygenases [LPMOs)] are a group of copper-dependent enzymes that play a role in the degradation of recalcitrant polysaccharides such as cellulose, chitin, hemicellulose, and pectin. These enzymes are found in a range of organisms, including bacteria, fungi, oomycetes, viruses, plants, and animals [1]. LPMOs catalyze the oxidation of crystalline and soluble polysaccharides using O_2 or H_2O_2 as co-substrates, resulting in polymer chain cleavage [2,3]. This process reduces crystallinity and increases wettability, thereby facilitating the enzymatic breakdown of these complex and recalcitrant biopolymers by glycoside hydrolases (GHs) [4,5]. Due to their important role in biomass degradation, LPMOs have received increasing attention in the last decade, particularly in the context of biofuel production and the development of sustainable biorefineries [6,7].

The Carbohydrate-Active EnZYme (CAZy) database classifies LPMOs into eight different Auxiliary Activity (AA) families (AA9 to AA11 and AA13 to AA17) [8], with each family having distinct structural and functional features. Among these families, AA16 is the least well characterized, despite being of particular interest due to its substrate specificity on cellulose and/or celloligosaccharides with C1 regioselective [9]. Lately, AA16 LPMO from *Myceliophthora thermophila* (now reclassified as *Thermothelomyces thermophilus*) was reported only to boost the oxidative activity of fungal AA9 LPMOs through the generation of H_2O_2, without demonstrating direct oxidative activity toward polysaccharides. This evidence challenged our understanding of whether AA16 truly qualifies as a *bonafide* LPMO [10]. On the other hand, the most recent publication for the same enzyme has reported oxidative activity towards xylan [11], putting a puzzle in this enigmatic family. Further, the AA16 LPMOs are primarily found in filamentous fungi and in oomycetes, where they can play a crucial role in the degradation of plant cell walls and act as phytopathogenic virulence factors [12,13]. In addition, AA16 LPMOs have been reported to boost the activity of cellulases and other carbohydrate-active enzymes, enhancing the efficiency of biomass degradation [9–12].

Despite the above-mentioned importance of AA16 LPMOs, information on their structure and function is still limited, particularly for those found in basidiomycetes. Previous work from our group has described a transcript encoding an AA16 (L)PMO, which was highly expressed in the marine and sponge-symbiont basidiomycete *Peniophora* sp. when cultivated under a laccase-inducing media. Transcripts from *Pn*AA16 were at the same expression level

as those from the sum of the five AA9 LPMOs expressed under the same growing conditions [14], triggering interest in studying this enzyme.

In this context, this study aimed to obtain biochemical and structural properties of *Pn*AA16. To achieve this goal, we employed a combination of molecular modelling, spectroscopy, and biochemical assays. Overall, the results described herein provide insights into the function and structure of LPMOs from the family AA16 and pave the way for future research into their biotechnological applications.

Materials and Methods

Sequence Retrieving, in silico and CDS Architecture Analysis.

The coding sequence (CDS) for *PnAA16* (VDC00504.1) was retrieved from the genome of the basidiomycete *Peniophora* CBMAI 1063 (PRJEB28379). The CDS was analyzed using the SignalP 6.0 server for signal peptide (SP) prediction against Eukarya as an organism group [15]. DeepLoc 1.0 server was also employed for protein cellular localization, using the "Profiles" accurate mode [16]. After, the *PnAA16* sequence was submitted to the SMART database for protein architecture analysis [17]. Taxonomic classification from AA16 homologous sequences was performed on the EFI (Enzyme Function Initiative Tools) website [18].

Phylogenetic Analysis

To identify orthologous sequences of *PnAA16*, the CDS was queried against the NCBI nr protein database using BLASTP analysis with default parameters. The CDS of LPMOs presenting functional or structural studies from the AA16 family and other LPMO families were also downloaded from the CAZy database. After retrieving those sequences, a search was conducted for SP sequences using the SignalP 6.0 platform, and sequences without a His residue after the SP cleavage site were removed.

Multiple sequence alignment was performed using T-COFFEE (Homology Extension PSI-coffee mode) in default parameters and without curation and with the His residue as the first amino acid of each sequence [19]. Jalview Version: 2.11.2.7 was used as an alignment visualization tool [20]. Maximum likelihood analyses were then conducted to gain insights into the phylogenetic relationships among the LPMOs belonging to the AA16 family, using the "a la carte" mode on www.phylogeny.fr [21] The alignment results from T-COFFEE were used to construct the phylogenetic tree using PhyML with default metrics, except for gaps, which were not removed from the alignment. Statistical tests for branch support were performed using the Approximate Likelihood-Ratio Test (aLRT) in the SH-like mode [21]. Finally, the phylogenetic tree was visualized using the iTOL web platform [22].

Molecular Modelling

To create a three-dimensional homology model of *Pn*AAA16a, the native signal peptide sequence was excluded, and the ColabFold v1.5.2: AlphaFold2

(https://colab.research.google.com/github/sokrypton/ColabFold/blob/main/AlphaFold2.ipynb), using MMseqs2 was utilized using the structure of *T. thermophilus* (G2QH80; PDB id.: 7ZE9) as template, followed by one round of relaxation using the Amber option [23,24]. The resulting five models were then subjected to pLDDT analysis, and the top-ranked model was chosen for ligand binding site prediction with the aid of COFACTOR and COACH tools, which integrated data on structure, sequence, and protein-protein interaction from the BioLiP database at I-TASSER web platform [25]. After, the model was statistically evaluated using the QMEANDisC*o* scoring function from the SWISS-MODEL web server [26]. PDB visualizations of the model were generated using the PyMOL™ software (1.7.4.5) [27]. Furthermore, the electrostatic surface potential was calculated with the Adaptive Poisson-Boltzmann Solver (APBS) [28] plug-in at pH 6.0 for PyMOL™.

Cloning and Recombinant Protein Expression

The CDS encoding *Pn*AA16 was synthesized by GeneScript (GenScript Biotech Corporation, New Jersey, United States). The CDS was cloned into the pET-26b(+) vector without the native signal peptide and the intrinsically disordered C-terminal region (dCTR), aiming for periplasmic expression [29]. The LPMO catalytic domain of *Pn*AA16 was added between the pelB leader signal peptide and the *BamH*I restriction site, and a strep-tag was inserted in the LPMO C-terminal, followed by a stop codon, therefore removing the 6xHis-tag from the vector construct. The plasmid was transformed into *E. coli* BL21(DE3) Rosetta 2 pLys S for protein production.

A single colony containing the desired construction was pre-inoculated in Lysogenic Broth (LB) and grown overnight at 37 ºC and 200 rpm. Next, 20 mL of the overnight culture was inoculated in 800 mL of 1x M9 minimal medium with 1% glucose as the sole carbon source and grown at 37 ºC and 220 rpm until the optical density reached 1.0. The cells were cooled to 16 ºC for 1 h, and protein expression was induced by adding Isopropyl β-d-1-thiogalactopyranoside (IPTG) to 1 mM final concentration. Recombinant protein production was carried out for 16-20 h at 16 ºC and 180 rpm [29,30].

After protein expression, *Pn*AA16 was extracted from the periplasm using the Osmotic Shock protocol and purified in 100 mM Tris-HCl pH 8.0, containing 150 mM NaCl, using affinity chromatography with Strep-Tactin ®XT resin. After elution using the same buffer containing 50

mM biotin, the *Pn*AA16 was concentrated, and copper ion ($CuCl_2$) was loaded in five-fold excess, followed by size-exclusion chromatography, using a Superdex 75 Increase 10/300 GL in 25 mM MES buffer at pH 6.5, with 150 mM NaCl, running as mobile phase [29,30].

Structural characterizations of PnAA16

The melting temperature (Tm) was determined using the protein thermal shift assay [31]. The copper-loaded *Pn*AA16, at a concentration of 0.2 mg/mL (20 mM MES pH 6, 150 mM NaCl), was combined with 1X SYPRO Orange in a reaction volume of 30 µL. To remove the copper ion from the protein structure, *Pn*AA16 was treated with 10 mM ethylenediamine tetraacetic acid (EDTA) for 2 h before the assays. Fluorescence emission (excitation at 470 nm; emission at 570 nm) was monitored using a CFX384 Touch Real-Time PCR machine (BioRad) in a 384-well clear plate. The temperature ranged from 20 °C to 99 °C, with a 2 min-incubation at each temperature before recording the output [30]. The process was performed in triplicate. Raw data points were analyzed in the JTSA web platform [32], using non-linear least squares regression, more specifically the Levenberg–Marquardt algorithm with the five-parameter sigmoid equation (Sigmoid-5). The curve midpoint was used to determine the protein Tm [33].

Circular dichroism (CD) spectra were obtained using a Jasco J-815 spectropolarimeter equipped with a temperature control device [34]. The concentration of *Pn*AA16 was 0.25 mg/mL in 20 mM MES buffer pH 6.5 in the absence and presence of copper ion. The experiments were conducted at 25 °C, employing a 0.1 cm quartz cuvette. Spectra were recorded eight times over the wavelength range of 195 to 260 nm after they were averaged to generate a final CD spectrum. The spectra were acquired using a scanning speed of 100 nm/min, a spectral bandwidth of 1 nm, and a response time of 0.5 s, with results obtained on a degree scale. The buffer background contribution was subtracted from each experiment.

The purified *Pn*AA16 was analysed using the Nano-ZS dynamic light scattering (DLS) system from Malvern Instruments Ltd, located in Malvern, UK. A protein solution at a 1 mg/mL concentration was prepared in 20 mM MES buffer adjusted at pH 6.5. The protein was loaded into a quartz cuvette before commencing the measurements. The temperature of the system was increased from 20 °C to 80 °C, and the samples were allowed to equilibrate for 5 min at each temperature before performing DLS measurements. Multiple records of the DLS profile

were collected during this process. Electrophoretic light scattering (ELS) was used to determine the average zeta potential (collected using a Zetasiser Nano-ZS) [35]. Zeta potential was measured at 1 mg/mL in 20 mM MES buffer adjusted at pH 6.5 and 25 ºC. Knowledge of electrophoretic mobility enables one to calculate the average number of charges per molecule from the Lorenz–Stokes relationship [36].

EPR spectra at X-band frequency (~9.3 GHz) were obtained using a Bruker micro EMX. The modulation amplitude was set to 4 G, with a modulation frequency of 100 kHz and a microwave power of 10.02 mW. The measurements were performed at a temperature of 165 K and the EPR spectra were recorded for a 0.15 mM solution of copper-loaded *PnAA16*. The spectra were collected in two conditions: (1) in the absence of cellohexaose and 150 mM NaCl, and (2) in the presence of excess cellohexaose and 150 mM NaCl, both in a 50 mM MES buffer at pH 6.0. The acquired spectra were simulated using Easy Spin 5.2.6 [37], which is integrated into MatLab 2016a software.

Biochemical characterization of PnAA16

The oxidase ability of *Pn*AA16 was evaluated using the Amplex®Red assay for H_2O_2 quantification. The experimental setup followed the protocol described by Kittl et al. (2012) [38], with triplicate samples prepared in a clear microplate with a final volume of 100 µL. Each assay consisted of 50 µM of various electron donors (ascorbic acid, pyrogallol, gallic acid, and L-cysteine), 50 µM Amplex®Red, 7 U/mL Horseradish peroxidase (HRP), and 1 µM LPMOs in 1x PBS pH 7.2. The reactions were initiated by adding the LPMOs, and the formation of the product (resorufin) was monitored by measuring absorbance at 590 nm. The kinetics of the reactions were recorded for 30 min or 60 min at 30 ºC using the Epoch 2 Microplate Reader (BioTek), with 3 s of shaking before each reading. The results were interpreted as stoichiometric, which the amount of peroxide produced (in µM) was divided by the amount of protein (µM) in the reaction. To quantify the H_2O_2 produced, a standard curve in the presence of each reductant was constructed using peroxide concentrations ranging from 0.1 to 10 µM.

The LPMO peroxidase activity assay using 2,6-dimethoxyphenol (2,6-DMP) and H_2O_2 as co-substrates, was conducted as described by Breslmayr et al. (2018) to account more physiological conditions [39]. The reactions were prepared in a total volume of 200 µL, with final concentrations of 0.1 mM H_2O_2, 10 mM 2,6-DMP, and 1 µM of LPMOs in a 100 mM ammonium acetate buffer at pH 6, maintained at 30 ºC. Additionally, assays were performed

by varying the H_2O_2 concentration within the range of 0.1 to 10 mM to evaluate whether the co-substrate concentration had influence in the overall specific activity of the enzyme. The LPMOs were mixed with all the other reagents, which were pre-incubated for 15 min at 30 ºC, to initiate the reaction. The absorbance was then measured at 469 nm every 15 s for a duration of 5 or 30 min, using the Epoch 2 Microplate Reader (BioTek) with the correction pathlength option enabled. LPMO activity was quantified based on the formation of coerulignone, with one unit of activity defined as the production of 1 µmol of coerulignone (ε_{469nm} = 53,200 $M^{-1}.cm^{-1}$) per min under the specified reaction conditions.

Evaluation of substrate specificity

The activity assays aiming to determine the *PnAA16* specificity for carbohydrate substrates were performed on a range of different polysaccharides: microcrystalline cellulose (Avicel), phosphoric acid swollen cellulose (PASC), squid pen chitin, xyloglucan (from tamarind, Megazyme), corn starch (Sigma) and xylan from oat spelt (Sigma); in addition to oligosaccharides such as cellohexaose (Megazyme), xylohexaose (Megazyme) and mannohexaose (Megazyme). Reactions were carried out in a final volume of 100 µL for 2, 6 and 16 h with substrate concentration of 10 mg/mL (polysaccharides) or 5 mg/mL (oligosaccharides) in 20 mM ammonium acetate buffer pH 6.0, 2 mM ascorbic acid as reductant and 1 µM of LPMO were added to the reactions, that were assayed at 30 °C and 950 rpm using a Thermomixer (Eppendorf). All assays were performed in triplicate. After centrifugation at 14,000*g* for 20 min, the supernatants were transferred to conical vials for analysis.

The HPAEC-PAD (High-Performance Anion Exchange Chromatography with Pulsed Amperometric Detection) analysis of polysaccharides and oligosaccharides was performed as previously described [40]. The analysis was conducted using an ICS-6000 system from Thermo Scientific, equipped with a disposable electrochemical gold electrode. For the analysis, 5 µL samples were injected into a CarboPac PA1 column (2 × 50 mm). The column was operated at a temperature of 30 °C and eluted with 0.1 M NaOH (eluent A) at a 0.25 mL/min flow rate. Separation of native, C1, C4, and C1/C4 oxidized oligosaccharides was achieved by employing a stepwise gradient with increasing concentrations of eluent B (0.1 M NaOH + 1 M NaOAc). The gradient elution conditions were as follows: 0-10% B from 0 to 10 min (curve 5); 10-16% B from 10 to 19 min (curve 6); 16-100% B from 19 to 25 min (curve 6); and 100% B from 25 to 30 min (curve 5). The column was then reconditioned with 0% B from

30 to 50 min. Chromatograms of the separated compounds were recorded using Chromeleon 7.0 software, allowing for data analysis and interpretation.

Saccharification assays

The saccharification of Avicel PH-101 (Sigma Aldrich, St. Louis, MO, USA) was performed in 2 mL screw cap microtubes with a 500 µL working volume, in triplicate. Each reaction contained 10 mg of substrate in 50 mM Sodium Acetate pH 5.0 at 30 °C, with agitation at 800 rpm using a Thermomixer. Celluclast® 1.5 L was added at a final concentration of 10 FPU/g of substrate, along with 0.05 mg of β-glucosidase (AnCel3A from *Aspergillus niger*) per reaction. Ascorbic acid, hydrogen peroxide, and *PnAA16* were included in the reactions when needed at final concentrations of 1 mM, 0.2 mM, and 0.01 mM respectively.

After 24 h, the reactions were halted by rapid cooling in ice, followed by centrifugation at 13,000*g* for 15 min at 4 °C. The diluted hydrolysates were then analyzed for glucose and cellobiose content using high-performance anion exchange chromatography with pulsed amperometric detection (HPAEC-PAD). For the analysis, 5 µL of each sample was injected into a CarboPac PA1 column (2 × 50 mm), which was operated at a temperature of 30 °C. The column was eluted isocratically with 0.03 M NaOH as the mobile phase at a flow rate of 0.25 mL/min for 15 min. After, the column was reconditioned with the same mobile phase for an additional 15 min. Glucose and cellobiose separation was achieved at retention times specific to each compound. A calibration curve was constructed using both saccharides to quantify the sugars. Chromatograms of the separated compounds were recorded using Chromeleon 7.0 software, which facilitated their quantification.

Results

CDS architecture and structural predictions

The coding sequence of *PnAA16* consists of 1,047 base pairs (bp) and encodes a mature protein comprised of 348 amino acid (a.a.) residues. A signal peptide (SP) of 20 residues (Met1-Gly20) was predicted with a high likelihood (0.99). Consistent with LPMOs, *PnAA16* featured a histidine residue immediately following the signal peptide. Using Protparam, the expected molecular weight of *Pn*AA16 (excluding the SP) was estimated to be 32.8 kDa, with a theoretical isoelectric point (pI) of 4.4. The extinction coefficient at 280 nm was estimated as 17,460 $M^{-1}.cm^{-1}$, assuming that all the pairs of cysteine (Cys) residues formed disulphide bridges. Deeploc 1.0 analysis indicated a high likelihood of 0.96 for *PnAA16* being an extracellular protein. The Smart database revealed that *Pn*AA16 has the Pfam *(L)PMO_10* (PF03067) domain at the N-terminus (residues from 21 to 188). Subsequently, a region with low complexity, known as the dCTR region [41], was identified (residues 192–306) (Figure 1A).

Phylogenetic analysis

A BLASTP search was conducted using the *Pn*AA16 amino acid sequence as the query, retrieving more than 900 orthologous coding sequences (CDSs) all of which belonged to the Fungi kingdom. Most sequences were classified as belonging to Ascomycetes, followed by Basidiomycetes. The most representative genera were *Fusarium* and *Aspergillus* (Fig. 1B). From those sequences, ten were selected for the phylogenetic analysis, with identities ranging from 85% to 20%. Additionally, three sequences corresponding to characterized AA16 LPMOs from *Aspergillus aculeatus* (A0A1L9X7U6), *Aspergillus nidulans* (AN0778.2), and *Thermothelomyces thermophilus* (G2QH80; PDB 7ZE9), were included in the analysis.

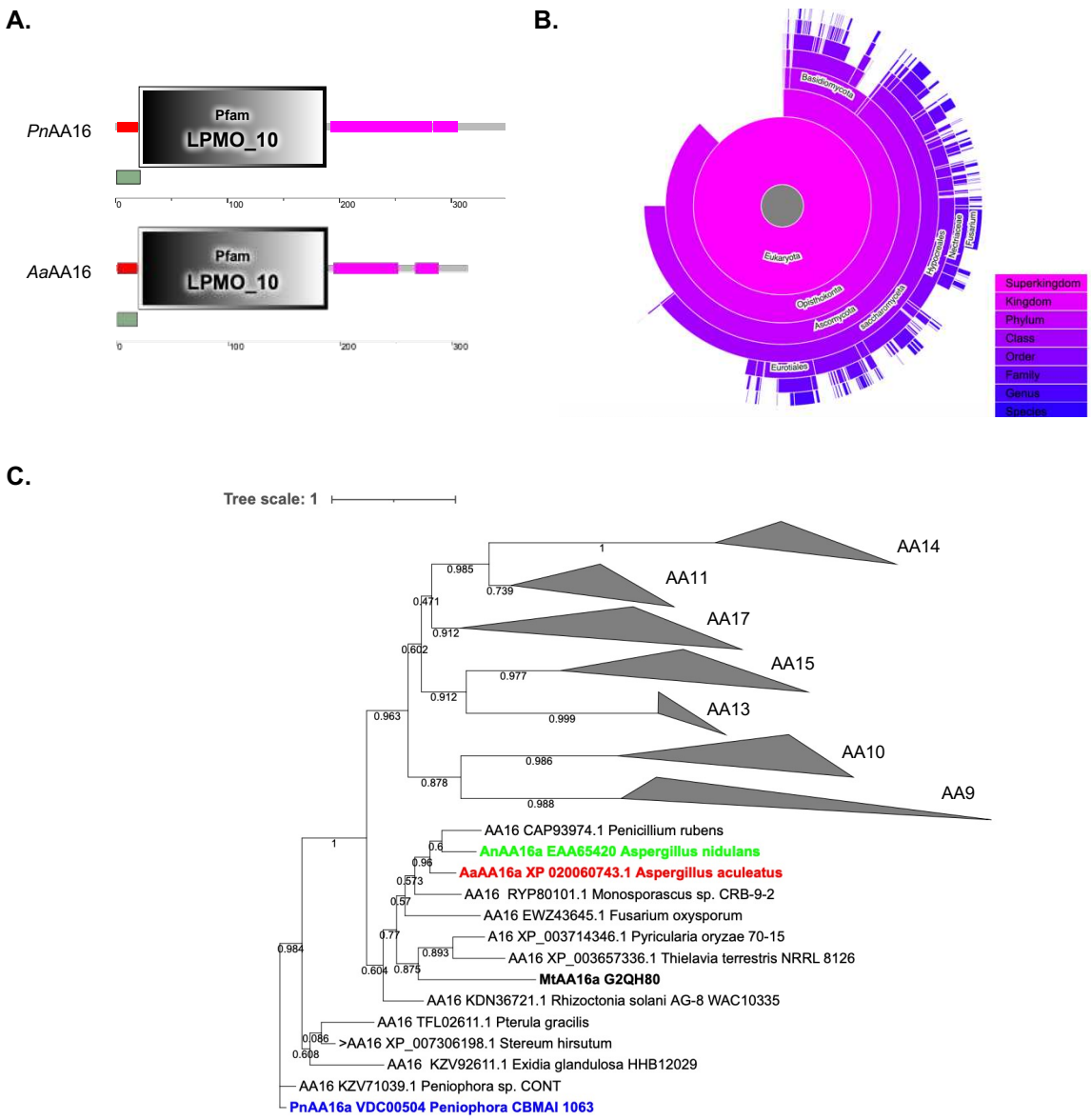

Figure 1. In-silico analyses of the full-length *Pn*AA16 amino acid sequence. (A) Protein architecture analysis from SMART Database. The signal peptide is highlighted in red, the (L)PMO_10 Pfam domain in black and the dCTR region in pink for both *Pn*AA16 and *Aa*AA16a sequences. **(B)** Taxonomic classification of AA16 homologous sequences. **(C)** Phylogenetic tree of LPMO families, highlighting the AA16 family branch.

Alignment of amino acid sequences was performed by T-COFFEE revealing the conservation of the His-brace motif and the presence of a Tyr residue in the Cu axial position of the second coordination sphere. The sequence alignment also exhibited the conservation of Ile or Ala residues, which occurs at the active site of AA16 LPMOs (Fig. S1). In addition, a deletion of around 10 amino acids was observed around position 50 for a group of proteins, which includes *Pn*AA16, followed by some amino acid insertions around positions 110 and 150 for the same group of proteins. Finally, a maximum likelihood analysis was carried out to

ascertain the phylogenetic relationships among the AA16 LPMOs, with LPMO sequences from other families employed as outgroups (Fig. 1C). The analysis demonstrated that AA16 LPMOs form a distinct cluster from other LPMO families. The AA16 LPMOs's phylogeny depicted two distinct branches. The first branch, supported by a bootstrap value of 0.64, primarily consisted of AA16 LPMOs from ascomycetes, except for one AA16 LPMO from the basidiomycete *Rhizoctonia solani*. In turn, the second branch of AA16 LPMOs exhibited a high bootstrap (1.0) and greater phylogenetic distance from other LPMO families and exclusively included enzymes from basidiomycetes. The *Peniophora* sp. LPMOs were positioned in an unassociated branch within the second clade (Fig 1C).

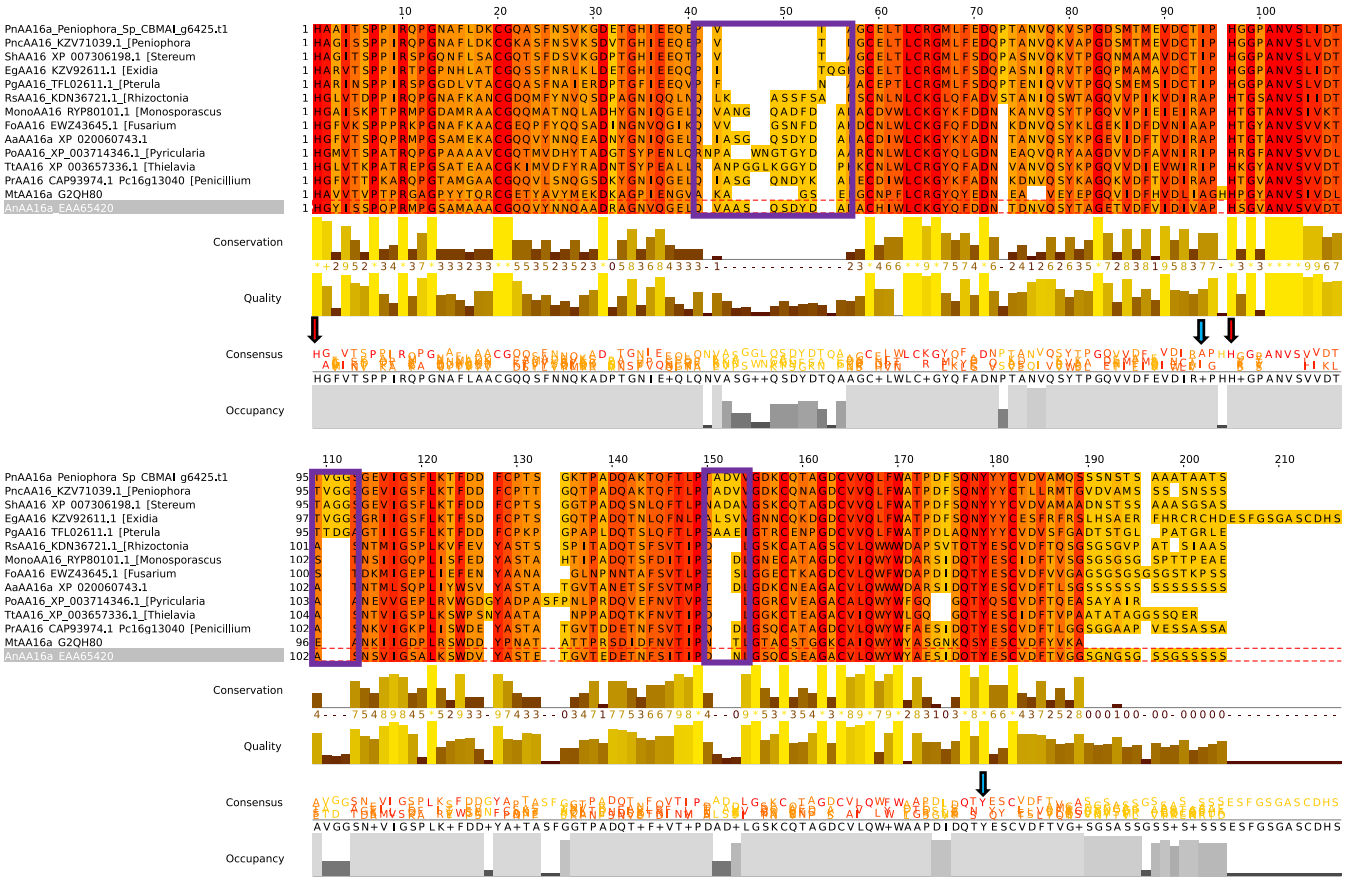

Supplementary Figure 1. Multiple sequences alignment (Homology Extension) of AA16 LPMOs. Purple lined boxes indicate major amino acid insertion and deletions among the AA16 sequences. The red and blue arrows show the alignment of consensus amino acids for the histidine-brace and the second-sphere environment from AA16 LPMOs respectively.

Structural insights of PnAA16 reveal hallmarks of an LPMO

To obtain structural information of *Pn*AA16, the enzyme was modelled using the AlphaFold 2 server without any structural template. Initially, a full-length model of *Pn*AA16 was generated, showing a high sequence coverage (Fig. 2SA) and high pLDDT score (approximately 95% confidence) (Fig. 2SA and B). However, the C-terminal dCTR region of *PnAA16* exhibited lower sequence coverage and pLDDT score (around 35%) (Fig. 2SA, B and E) due to limited sequence identity as previously reported in AA9 LPMOs [41]. Consequently, a new modelling approach was employed, focusing on the amino acid sequence of the N-terminal catalytic core. The resulting relaxed three-dimensional homology model of *PnAA16* exhibited a favourable pLDDT score of 95% (Fig. S2C, D and F). To further validate the model, a TM-align analysis was performed in the I-TASSER server using the structure of AA16 LPMO from *T. thermophilus* (G2QH80; PDB id.: 7ZE9) as a template. The TM-score, ranging from 0 to 1, was calculated as 0.90, with an estimated RMSD of 1.48 Å.

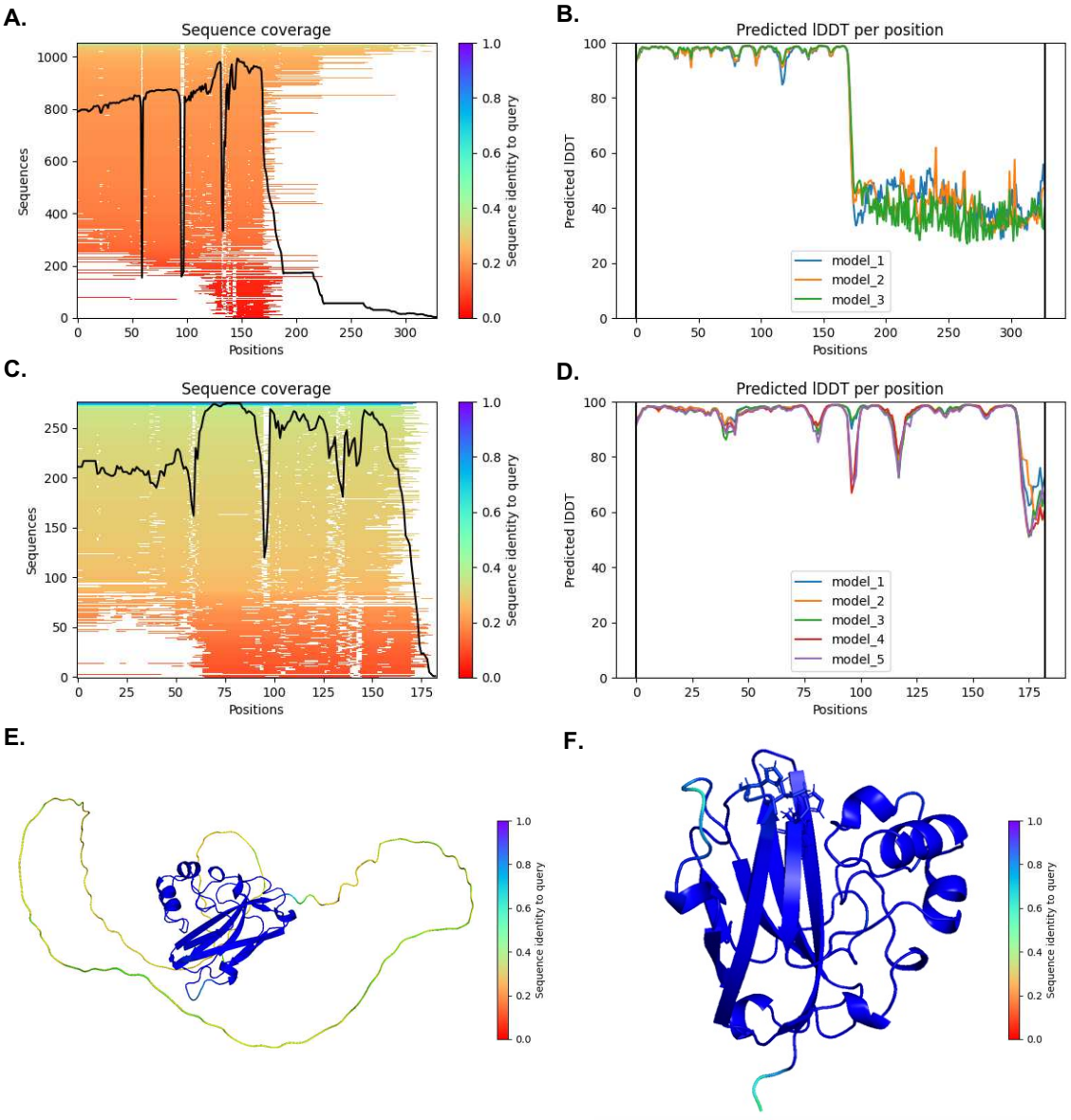

Supplementary Figure S2. *Pn*AA16 prediction metrics from AlphaFold 2. (A) *Pn*AA16 full-length sequence coverage from the PDB database. **(B)** pLDDT score per amino acid position of *Pn*AA16 full-length sequence. **(C)** *Pn*AA16 catalytic core sequence coverage from the PDB database. **(D)** pLDDT score per amino acid position of *Pn*AA16 catalytic core sequence. **(E)** Relaxed and ranked 1 cartoon model for *Pn*AA16 full-length. The structure was coloured according to the pLDDT score. **(F)** Relaxed and ranked 1 cartoon model for *Pn*AA16 catalytic. The structure was coloured according to the pLDDT score.

The homology model of the N-terminal domain of *PnAA16* exhibits the characteristic structure of LPMOs, featuring a central and antiparallel β-sandwich fold connected by several loops. The stability of these loops is augmented by four disulphide bonds (Fig. 2A), which align with the structure of *Mt*AA16a (PDB id: 7E9Z). The model of *PnAA16* indicates the presence of a copper ion in the active site, with a C-Score of 0.58 as determined by the COFACTOR and COACH tools of the I-TASSER server. Conserved residues His1 and His83 are predicted to

coordinate the ion in the T-shaped pocket (Fig. 2B), similar to other structurally characterized LPMOs [8]. The axial position of the copper ion is occupied by a Tyr, while an Ile81 residue occupies a region in the axial secondary coordination sphere of the ion (Fig. 2B). Previous studies have suggested that hydrophobic and polar charged residues surrounding the active site and exposed to the solvent on the flat catalytic surface of LPMOs, play a role in substrate binding [42,43]. For *Pn*AA16, these solvent-exposed residues were also found on its binding surface, encircling the His-brace, such as the hydrophobic residues Ile81 and Phe158, along with polar residues such as Asp31, His35 Glu38, Glu40, Asp157, and Gln160 (Fig. 2C). In addition, the molecular surface of *PnAA16* model was used to generate the electrostatic potential at pH 6, revealing an overall negative charge for the enzyme (Fig. 2D).

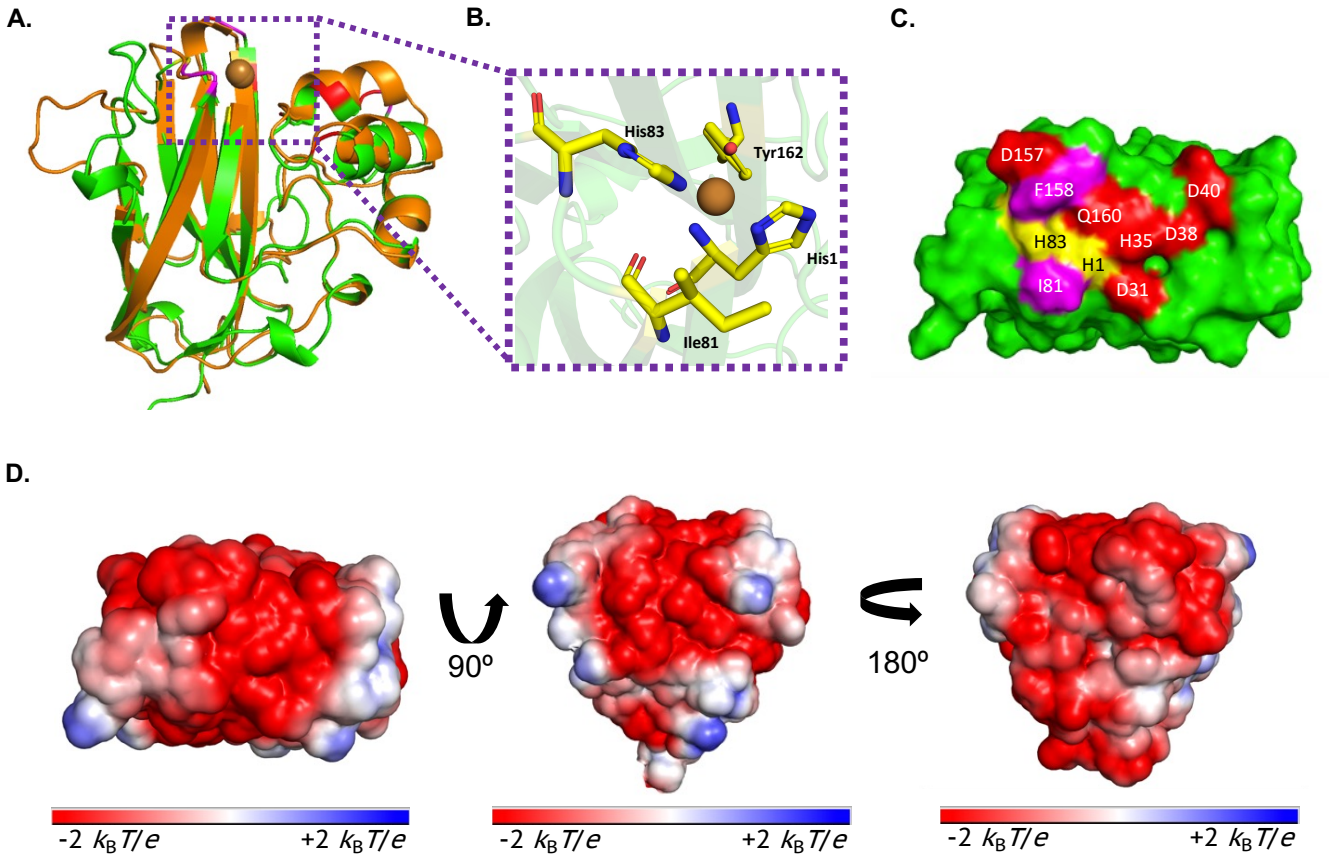

Figure 2. Structural features of *Pn*AA16. (A) Cartoon representation of the three-dimensional (3D) homology model of *Pn*AA16 (green) superimposed with the 3D molecular structure of *Mt*AA16a PDB id: 7E9Z (orange). **(B)** Detail of the histidine-brace and second sphere residues around the copper environment. **(C)** The flat catalytic surface of *Pn*AA16 shows the hydrophobic residues in pink, the polar charged in red and the his-brace in yellow. **(D)** Electrostatic surface potential of *Pn*AA16 set to -/+ 2 kT/e.

Recombinant production and spectroscopy studies of PnAA16

To obtain structural and functional information on *Pn*AA16, its catalytic domain was synthesized and cloned into a bacterial expression vector pET-26b(+) without the signal peptide (SP) and with a C-terminal Strep-tag II. Therefore, the expected molecular mass of the *PnAA16* LPMO domain (without SP and dCTR) was predicted as 19.5 kDa, with a theoretical pI of 4.41. An extinction coefficient of 17,460 $M^{-1}.cm^{-1}$ at 280 nm was calculated based on the amino acid sequence, assuming that all pairs of Cys residues form cystines. The recombinant expression in the periplasm and purification of the N-terminal portion of *Pn*AA16 (catalytic domain) were carried out as described previously with slight modifications [30]. Briefly, *Pn*AA16 was successfully produced in the *E. coli* periplasm, however, its soluble form could only be achieved when cultivation was performed using an M9 minimal medium without adding copper ions for supplementation. *Pn*AA16 was then purified by a two-step protocol employing both osmotic shock and affinity chromatography, and its purity was checked by SDS-PAGE (Figure S3A). Protein identity was confirmed by LC-MS/MS analysis of the protein band excised from SDS-PAGE and using blotting with an anti-Strep-tag antibody (data not shown). The *Pn*AA16 was copper-loaded to maintain stability, and any useable-unbound copper ion in excess were removed using size-exclusion chromatography (Figure S3B).

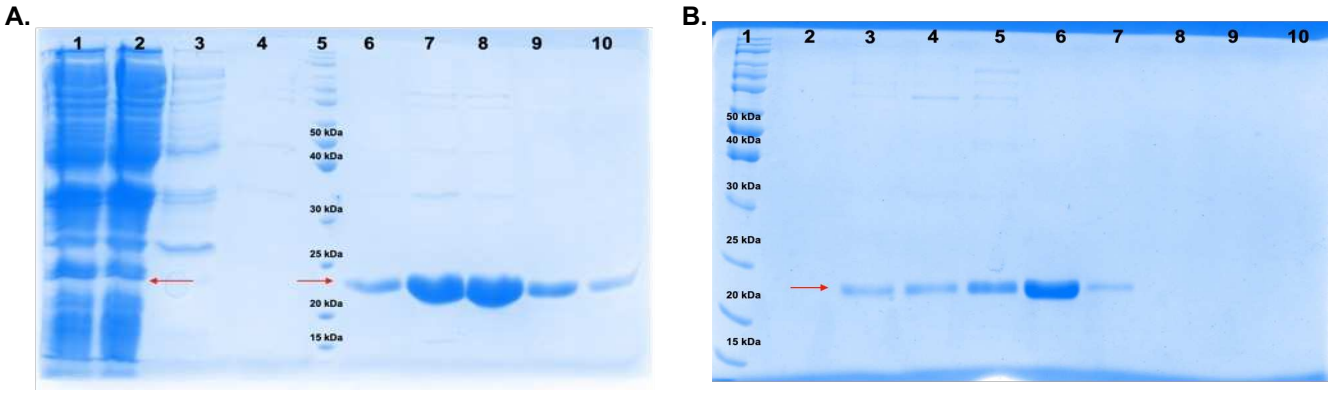

Supplementary Figure S3. **SDS-PAGE analysis of *Pn*AA16 purification. (A)** Strep-Tactin affinity chromatography fractions loaded in the12% SDS-PAGE. 1 – lysate, 2 – Flowthrough, 3-4 wash fractions, 5 – ladder, 6-10 eluted fractions with 50 mM biotin **(B)** Size-exclusion chromatography fractions loaded in the12% SDS-PAGE from copper loaded form of *Pn*AA16. 1 – ladder, 2 – void volume, 3-4 – 1st peak of elution, 5-7 – 2nd peak of elution.

To obtain information about thermostability, *Pn*AA16 was analysed in the absence and presence of copper ion using the thermofluor method with SYPRO Orange as the dye (Fig. 3A). Copper-loaded *Pn*AA16 exhibited a temperature of melting (T_m) of 72.5 ºC as compared

to 67.6 ºC after copper removal using EDTA (ΔT_m of 4.9 ºC). In turn, the shift in T_m from the *apo*-form *PnAA16* indicates that the copper ion provides a thermostabilizing effect to the protein structure, as previously reported for other LPMOs from different families [44,45]. The UV-visible spectrum measured for purified *Pn*AA16 at pH 6.5 lacked significant absorbance around 600 nm, indicating that the protein was purified in its *apo*-form (inset of Fig. 3B). The circular dichroism (CD) spectrum of purified *Pn*AA16 was typical of proteins containing β-sheets (black line Fig. 3B), similar to that reported for other fungal LPMOs as AA9 from *Neurospora crassa* [46] and *T. thermophilus* [47]. In the presence of copper ions, the spectrum of *Pn*AA16 was altered, indicating that the ion binding induces conformational changes in the protein structure (red line Fig. 3B), a behaviour consistent with findings reported for the AA9 LPMO from *N. crassa* [46].

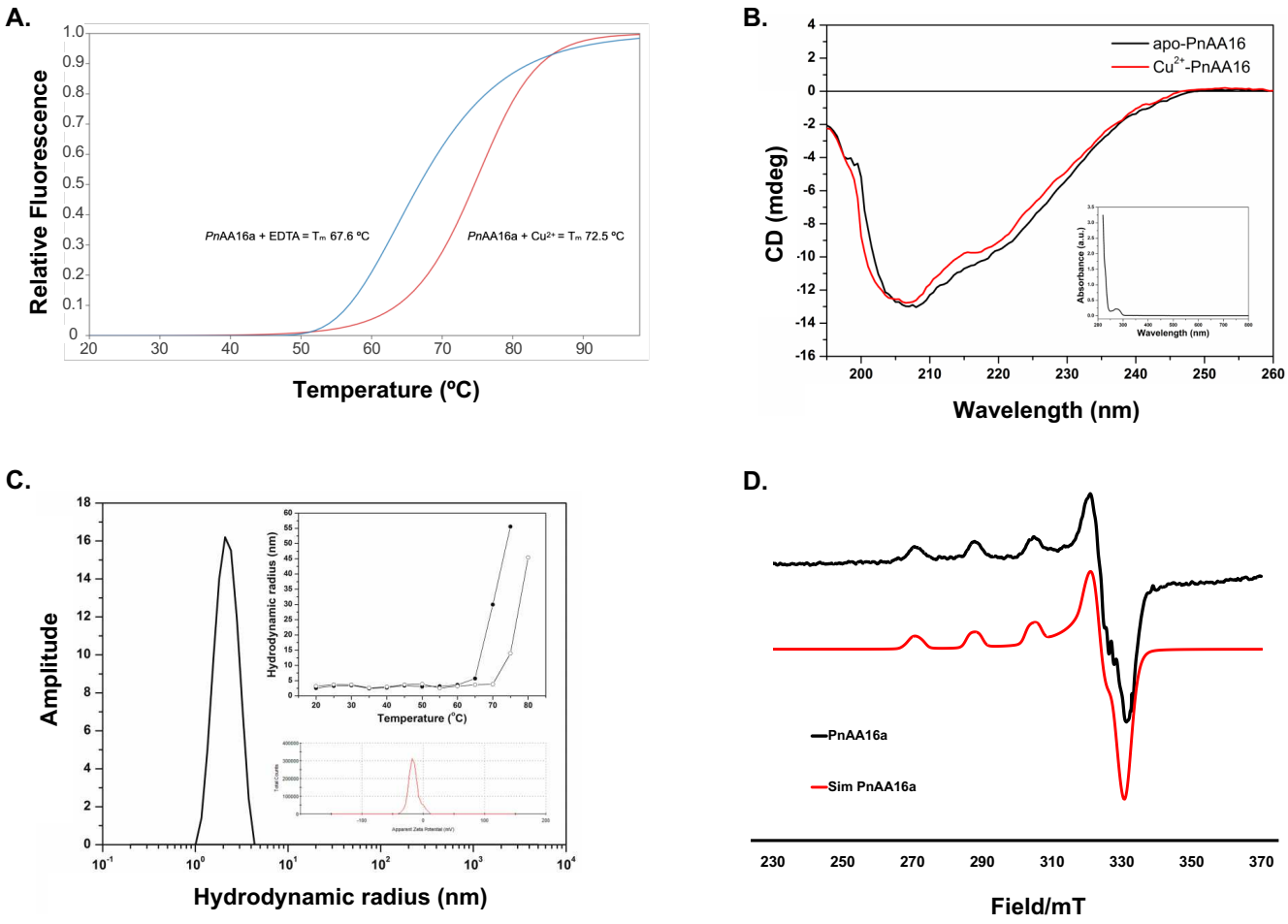

Figure 3. Spectroscopy analysis of *Pn*AA16. (A) Thermal shift curve of *Pn*AA16 at pH 6.0. The fluorescence was monitored, and raw data was used to extract the apparent melting temperature (Tm). The protein concentration was 0.2 mg/mL and the heating rate was 2°C/min. **(B)** Circular dichroism (CD) spectrum was measured for recombinant *Pn*AA16 at pH 6.5 (25 ºC) in the absence (black solid line) and presence of cooper ion (red solid line). Inset: UV-vis

spectrum for the recombinant *Pn*AA16 after purification steps. **(C)** DLS size distribution profile for *Pn*AA16. Above inset: the hydrodynamic radius of *Pn*AA16 at pH 6.5 as a function of temperature in the absence (black circle) and presence (open circle) of copper ions. Below inset: the zeta potential (below) for purified apo *Pn*AA16 at pH 6.5. **(D)** Frozen solution X-band CW-EPR spectra (165 K) of *Pn*AA16 (Experimental data in black, simulations in red).

The DLS profile measured for *Pn*AA16 at pH 6.5, in the absence or presence of copper ions was typical of a monodisperse solution corresponding to a hydrodynamic radius (R_H) of approximately 2.5 ± 0.3 nm (Fig. 3C). This value corresponds to a molecular mass of 28.7 ± 8.1 kDa assuming a spherical protein, most likely corresponding to a monomer with expected theoretical molecular mass of 21.8 kDa (considering the C-terminal Strep-tag II). In the absence of copper ion, the R_H of *Pn*AA16 exhibited minimal temperature dependence over the range 20 °C to 60 °C at pH 6.5 (inset of Figure 3C top), however at temperatures above 60 °C the R_H increased significantly suggesting a propensity for the protein to form amorphous aggregates. In contrast, in the presence of copper ions, the R_H increased significantly above 70 °C (inset of Figure 3C top). These results indicate that copper ion interaction causes conformational changes conferring a thermostabilizing effect on the protein structure. The copper thermostabilizing effect was also confirmed by thermofluor assay (Figure 3A). Consistent with the expected structural model, the theoretical pI value calculated from the amino acid sequence for *Pn*AA16 was 4.49 (with the C-terminal Strep-tag II), indicating that at pH 6.5 the protein structure is negatively charged. Indeed, the experimental zeta potential measured for *apo*-form *Pn*AA16 at pH 6.5 was - 15.8 ± 2.4 mV (inset of Figure 3C bottom), giving an average number of uncompensated charges per molecule of – 5.1 ± 0.9.

CW-EPR X-band spectroscopy was employed to determine the electronic state of the copper centre at the active site of *PnAA16* (Fig. 3D). The simulated spin-Hamiltonian parameters (g_I, g_{II}, g_{III} of 2.06, 2.06, 2.25 respectively and A_{III} 520 MHz) revealed axial characteristics ($g_x \approx g_y < g_z$) with a $d(x^2-y^2)$ singly occupied molecular orbital (SOMO), categorizing the copper active site as a type 2 site. These spin-Hamiltonian parameters closely resemble those obtained for AA9, AA14, and AA15 LPMOs [48], confirming the presence of a copper(II) ion within the His-brace coordination environment.

Biochemical characterization confirmed that PnAA16 can oxidize celloligosaccharides.

Previous reports have validated that LPMOs exhibit the capability to generate hydrogen peroxide (H_2O_2), when exposed to molecular oxygen and an external electron donor without

substrate, referred to as their oxidase activity [49]. Considering this characteristic, *Pn*AA16 was tested with various electron donors to investigate the range of molecules capable of reducing the copper ion at the (L)PMO's active site. Consequently, the Amplex®Red assay for H_2O_2 quantification was conducted at pH 7.0 and 30 ºC. The highest enzyme-induced H_2O_2 production was achieved by employing ascorbic acid as the external electron donor, generating over 5 µM of H_2O_2 per µM of the enzyme after a 15-minute reaction (Fig. 4A). When comparing the oxidase ability of *Pn*AA16 with that of LPMO AA9 from *A. nidulans* (protein ID: AN6428) [50], the production of H_2O_2 by *Pn*AA16 exhibited a lower initial velocity but eventually reached similar levels after 1 h of the reaction (inset of Fig. 4A top). Furthermore, in the presence of ferulic acid, gallic acid, and pyrogallol, the generation of H_2O_2 was also observed for *Pn*AA16, albeit at low levels compared to the AA9 from *A. nidulans*.

Figure 4. Biochemical features of *Pn*AA16. (A) Apparent hydrogen peroxide production of *Pn*AA16, using several electron donors for 30 min and 30 ºC; Top inset: time course of apparent hydrogen peroxide productions by *Pn*AA16 and *AN*6428 from *A. nidulans* for 60 min and 30 ºC; **(B)** Consumption of H_2O_2 determined by the formation of coerulignone from 2,6-DMP at 30 °C for 5 min. Top inset: Consumption of H_2O_2 determined the formation of coerulignone from 2,6-DMP at 30 °C for 5 min, varying protein concentrations. **(C)** Time-course (2, 6, 16 hours) HPAEC-PAD chromatograms of product mixtures from *Pn*AA16 reactions with cellohexaose (C6). Reaction products from C6 were native, C1- and C4-oxidized celloligosaccharides as

indicated in the top inset. All reactions were performed in triplicate, resulting in the same profile. **(D)** Avicel saccharification yields in the presence of Celluclast, with or without *Pn*AA16 and its co-substrates.

The peroxidase activity was also assessed using the 2,6-dimethoxyphenol (2,6-DMP) assay at pH 6.0 and 30 ºC (Fig. 4B), as previously described. It is important to note that this assay provides only approximate information about the peroxidase activity of LPMOs and does not necessarily correlate with oxidative activity on polysaccharides. The peroxidase-specific activity determined for Pn*AA16* on 2,6-DMP was found to be 0.27 ± 0.04 U/g, which is lower when compared to the fungal AA9 (AN6428) [39,50] (Fig. 4B). The peroxidase activity of Pn*AA16* was also examined via a dose-response assay, revealing a linear increase in peroxidase activity; however, the activity remained notably low (inset of Fig. 4B top). Additionally, varying the concentration of H_2O_2 from 0.1 mM to 6 mM (Fig. S4) resulted in a linear increase in activity, nevertheless, it remained at a low specific activity level.

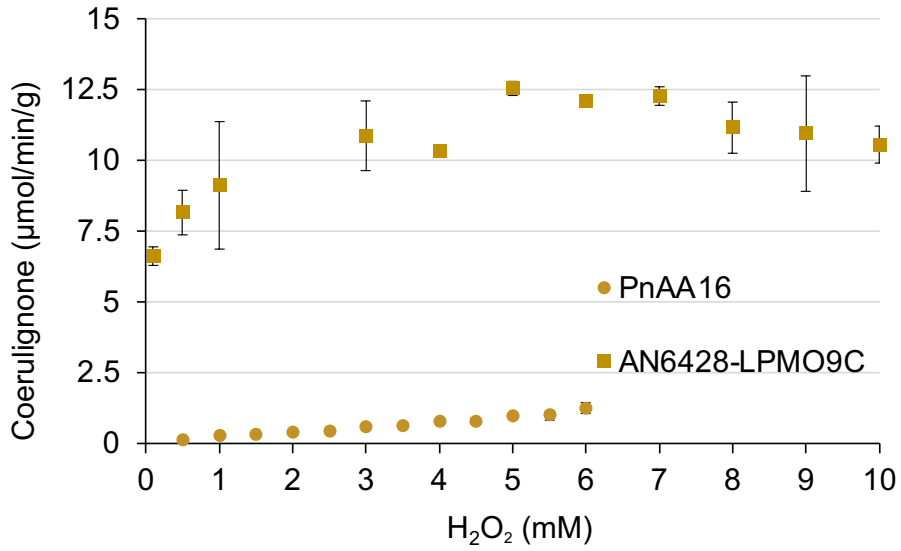

Supplementary Figure S4. **Hydrogen peroxide kinetics for *Pn*AA16a.** Consumption of different concentrations of H_2O_2 determined by the formation of coerulignone from 2,6-DMP at 30 °C for 30 min.

To investigate the substrate specificities of *PnAA16*, we conducted enzymatic activity assays at pH 6.0 and 30 ºC, utilizing a diverse array of polysaccharides (including Avicel, PASC, β-chitin from squid pen, xylan from oat spelt, xyloglucan from tamarind, starch from corn, pectin from citrus, cellohexaose, xylohexaose, chitohexose, and mannohexose) as substrates, with ascorbic acid serving as the external electron donor. The resulting reaction products were subjected to analysis by HPAEC-PAD after 2, 6, and 16 h of enzymatic assays.

PnAA16 exhibited activity exclusively on cellohexaose when in the presence of an external electron donor and molecular oxygen, displaying either a C1 or C4-oxidation pattern (Fig. 4C). Native celloligosaccharides, ranging from DP2 to DP5 (degree of polymerization - DP), were detected at retention times (RT) of approximately 10 to 19 min, followed by C1-oxidized peaks, between 19 to 25 min, and C4-oxidized peaks, between 25- and 30-min (inset fig. 4C). There was also the increase of the cellohexaose peak after 6 and 16 hours of reaction due to the co-elution of this oligosaccharide with cellobionic acid, as can be seen by the appearance of a shoulder in the C6 peak after 16 hours of reaction with ascorbate and *Pn*AA16. Furthermore, the notable increase in DP2 to DP4 peak intensities throughout the experiment provided further support for the enzymatic activity towards cellohexaose (inset of Fig. 4C top). EPR was also applied to investigate a possible interaction of cellohexaose with the copper 2+ centre of Pn*AA16*, however, no significative changes in the spectra were found (Fig. S5).

To assess the contribution of *Pn*AA16 to the saccharification of Avicel by a cellulase mixture (Celluclast + β-glucosidase), we quantified the yields of glucose and cellobiose generated through the synergistic action of these enzymes using HPAEC-PAD. Under our experimental conditions, the supplementation of ascorbate to the cellulolytic cocktail increased sugar yield by 20% in comparison to the cocktail alone (Fig. 4D). In the presence of *Pn*AA16 and ascorbate, the increment in sugar yields was approximately 50%, indicating a boosting effect of 30% for the cellulolytic activity on cellulose degradation in the presence of *Pn*AA16. The addition of only hydrogen peroxide to the Celluclast mixture did not enhance the saccharification of Avicel. However, a boosting effect was observed when PnAA16 and peroxide were present in the reaction, resulting in 50% increase in saccharification yields, similar to the effect of *Pn*AA16 and ascorbate. Interestingly, the addition of hydrogen peroxide to the cellulase mixture in the presence of ascorbate and *Pn*AA16 slightly reduced the boosting effect when compared with reactions using the standalone co-factors, probably due to enzyme inactivation (Fig. 4D). Definitively, these results underscored an enhancement of 30% and 50% in the activity of the cellulase mixture when the *Pn*AA16 and one of the co-substrates were present alone in the reaction, promoting a boosting effect of cellulases in the saccharification of crystalline cellulose.

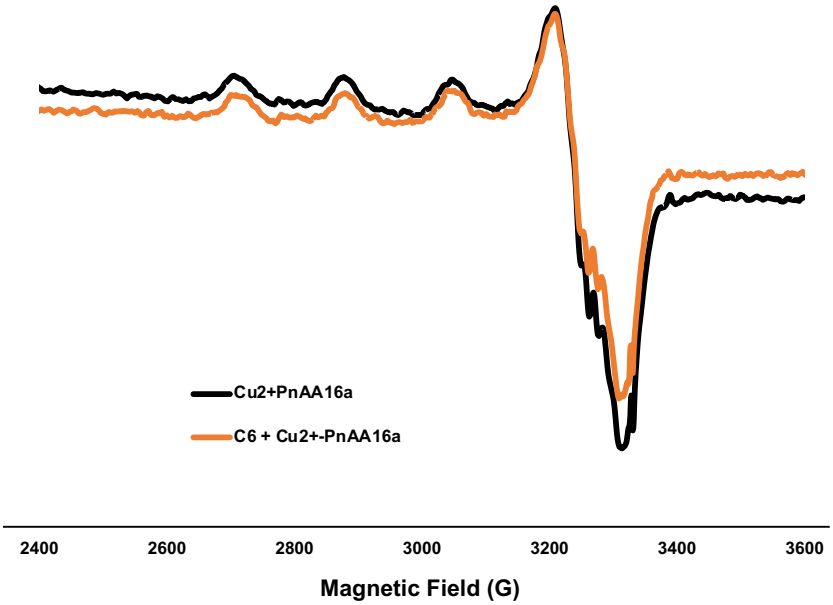

Figure S5. Frozen solution X-band CW-EPR spectra of *Pn*AA16 in the presence and absence of cellohexaose (C6).

Discussion

Over a decade since their discovery, LPMOs have become a class of enzymes that captivates interest due to their intrinsic ability to oxidize polysaccharides [2,51]. The enzymatic mechanism relies on a copper ion stabilized by the His-brace motif in (L)PMO's active site [2,52]. In 2019, Filiatrault-Chastel et al. reported the first description of the AA16 family LPMO identified in the secretome of five *Aspergillus* spp. grown on lignocellulosic biomass [9]. One AA16 protein from *A. aculeatus* (AaAA16) was biochemically characterized and exhibited oxidative activity on PASC with a C1 regioselectivity. Accordingly, the present study also demonstrated the C1 oxidative activity of *PnAA16* on cellohexaose. Furthermore, they revealed that *Aa*AA16 could act in synergy with cellobiohydrolase I (CBHI) from *Trichoderma reesei* for crystalline cellulose degradation [9], analogous to *Pn*AA16's boosting effect in Avicel presented herein. Notably, unlike *Aa*AA16, the *Pn*AA16 reported here can also oxidize cellohexaose at the C4 position.

A study involving two AA16 LPMOs (*Mt*AA16A and *An*AA16) from the ascomycete fungi *T. thermophilus* and *A. nidulans* reported that both enzymes were unable to oxidize various polysaccharides [10]. This extensive work further demonstrated that *Mt*AA16A can enhance the oxidative activity of AA9 LPMOs from *M. thermophila* by the generation of hydrogen peroxide, thereby stimulating peroxygenase activity in cellulose degradation. However, this effect was not observed when AA9 LPMOs from *N. crassa* were incubated with *Mt*AA16A [10]. The same study also reported the first molecular structure of an AA16 family member. Molecular modelling of *Pn*AA16 revealed a similar protein fold to the *Mt*AA16A structure but with slight differences in the composition of the residues displayed on the flat catalytic surface of both enzymes. These variations may explain their differing observed catalytic activities [10]. On the other hand, the most recently published work on AA16s described the heterologous expression and biochemical characterization of the same *T. thermophilus* (L)PMO, revealing oxidative activity toward xylan from birchwood [11], suggesting that *Mt*AA16A is a *bonafide* (L)PMO.

Furthermore, the LPMO *Mo*AA16a from the ascomycete *Magnaporthe oryzae* was also fully characterized [12]. The authors suggested that *Mo*AA16a can play a role in the virulence of the fungus during rice infection due to its high gene expression in the early stages of infection. After heterologous expression and purification, mature *Mo*AA16 was able to cleave

PASC with C1 regioselectivity, primarily generating native celo-oligos DP2, DP3, and DP4, followed by gluconic and cellobionic acids to a lesser extent [12]. This is consistent with the results obtained here for oxidation of cellohexaose as well as with *Aa*AA16 on PASC [9].

It is worth noting that the cellulose oxidation activity of all LPMOs AA16 reported so far is low [9,12] when compared to other LPMOs active on cellulose, such as those from families AA9, AA10, and AA15 [30,44,50,53]. These findings strongly hypothesized that cellulose may not be the preferential polysaccharide substrate for these AA16 LPMOs. It may depend on an unknown co-factor (metal or ion) or another co-substrate in addition to O_2/H_2O_2 to achieve their optimal catalytic performance. A fact is that the present work and the literature [9,11,12] collectively demonstrate that enzymes classified as AA16 are indeed LPMOs, as they can cleave and oxidize saccharide moieties, whether cello-oligos or soluble celluloses and also xylan. Furthermore, the three enzymes *Pn*AA16, *Aa*AA16, and *Mo*AA16 can enhance the cellulase activity against crystalline cellulose, which is another characteristic that qualifies AA16 as a *bonafide* (L)PMO. In specific, *Pn*AA16 boosts the cellulase cocktail activity by acting on the celloligosaccharides released by the action of endoglucanase on the crystalline cellulose.

In conclusion, our study reports the biochemical and structural characterization of *PnAA16,* an LPMO belonging to the AA16 family from a white-rot marine basidiomycete fungus, which displays the ability to cleave and oxidize cello-oligosaccharides. It is well-known that white-rot fungi are poor cellulose degraders due to the absence of key cellulases in their genome [54]. Therefore, it is reasonable to suggest that *PnAA16* does not have a role in crystalline cellulose oxidation but rather is capable of oxidizing short celloligosaccharides and boosting complex enzymatic mixtures for cellulose degradation. Collectively, this study sheds light on the enigmatic AA16 family by providing valuable structural and functional insights into *Pn*AA16. These findings broaden our understanding of LPMO diversity and potentially pave the way for future applications of this enzyme family.

CRediT authorship contribution statement.

JPLFC conducted the experiments, analysed the data, conceptualized the work, and wrote the draft and the final versions of the manuscript. **DVA** conducted the experiments and analysed the data. **VBA** conducted the experiments and analysed the data. **CRFT** conducted, analyzed, and conceptualized the experiments. **AT** conducted and analyzed experiments. **TAG**

conducted and analyzed experiments. **DD** conducted and analyzed experiments. **FLF** conducted and analyzed experiments. **LBB** conducted and analyzed experiments. **PHW** conceptualized experiments and reviewed the manuscript. **ARLD** conceptualized experiments, supervised the work and reviewed the manuscript. **WG** analyzed the data, conceptualized experiments, and wrote the draft and final versions of the manuscript. **FMS** conceptualized and supervised the work and wrote the draft and the final versions of the manuscript.

Acknowledgements

This study was funded by Fundação de Amparo à Pesquisa do Estado de São Paulo (FAPESP) via grant numbers: 2016/09950-0; 2015/50590-4; 2020/05784-3; 2017/17275-3; 2018/13500-5 also by Conselho Nacional de Desenvolvimento Científico e Tecnológico (CNPq) via grant numbers FMS 428527/2018-3 and 306279/2020-7; WG 305740/2017-2; 422132/2018-7 and 305816/2020-9.

References

[1] T.M. Vandhana, J.-L. Reyre, D. Sushmaa, J.-G. Berrin, B. Bissaro, J. Madhuprakash, On the expansion of biological functions of lytic polysaccharide monooxygenases, New Phytologist 233 (2022) 2380–2396. https://doi.org/10.1111/nph.17921.

[2] R.J. Quinlan, M.D. Sweeney, L. Lo Leggio, H. Otten, J.-C.N. Poulsen, K.S. Johansen, K.B.R.M. Krogh, C.I. Jorgensen, M. Tovborg, A. Anthonsen, T. Tryfona, C.P. Walter, P. Dupree, F. Xu, G.J. Davies, P.H. Walton, Insights into the oxidative degradation of cellulose by a copper metalloenzyme that exploits biomass components, Proceedings of the National Academy of Sciences 108 (2011) 15079–15084. https://doi.org/10.1073/pnas.1105776108.

[3] B. Bissaro, Å.K. Røhr, G. Müller, P. Chylenski, M. Skaugen, Z. Forsberg, S.J. Horn, G. Vaaje-Kolstad, V.G.H. Eijsink, Oxidative cleavage of polysaccharides by monocopper enzymes depends on H 2 O 2, Nat Chem Biol 13 (2017) 1123–1128. https://doi.org/10.1038/nchembio.2470.

[4] T. Uchiyama, T. Uchihashi, T. Ishida, A. Nakamura, J.V. Vermaas, M.F. Crowley, M. Samejima, G.T. Beckham, K. Igarashi, Lytic polysaccharide monooxygenase increases cellobiohydrolases activity by promoting decrystallization of cellulose surface, Science Advances 8 (2022) eade5155. https://doi.org/10.1126/sciadv.ade5155.

[5] D. Cannella, N. Weiss, C. Hsieh, S. Magri, M. Zarattini, J. Kuska, N. Karuna, L.G. Thygesen, I. Polikarpov, C. Felby, T. Jeoh, H. Jørgensen, LPMO-mediated oxidation increases cellulose wettability, surface water retention and hydrolysis yield at high dry matter, Cellulose 30 (2023) 6259–6272. https://doi.org/10.1007/s10570-023-05271-z.

[6] S. Srivastava, U. Jhariya, H.J. Purohit, N.A. Dafale, Synergistic action of lytic polysaccharide monooxygenase with glycoside hydrolase for lignocellulosic waste valorization: a review, Biomass Conv. Bioref. 13 (2023) 8727–8745. https://doi.org/10.1007/s13399-021-01736-y.

[7] M. Moon, J.-P. Lee, G.W. Park, J.-S. Lee, H.J. Park, K. Min, Lytic polysaccharide monooxygenase (LPMO)-derived saccharification of lignocellulosic biomass, Bioresource Technology 359 (2022) 127501. https://doi.org/10.1016/j.biortech.2022.127501.
[8] M.-L. Garron, B. Henrissat, The continuing expansion of CAZymes and their families, Current Opinion in Chemical Biology 53 (2019) 82–87. https://doi.org/10.1016/j.cbpa.2019.08.004.
[9] C. Filiatrault-Chastel, D. Navarro, M. Haon, S. Grisel, I. Herpoël-Gimbert, D. Chevret, M. Fanuel, B. Henrissat, S. Heiss-Blanquet, A. Margeot, J.-G. Berrin, AA16, a new lytic polysaccharide monooxygenase family identified in fungal secretomes, Biotechnology for Biofuels 12 (2019) 55. https://doi.org/10.1186/s13068-019-1394-y.
[10] P. Sun, Z. Huang, S. Banerjee, M.A.S. Kadowaki, R.J. Veersma, S. Magri, R. Hilgers, S.J. Muderspach, C.V.F.P. Laurent, R. Ludwig, D. Cannella, L. Lo Leggio, W.J.H. van Berkel, M.A. Kabel, AA16 Oxidoreductases Boost Cellulose-Active AA9 Lytic Polysaccharide Monooxygenases from Myceliophthora thermophila, ACS Catal. 13 (2023) 4454–4467. https://doi.org/10.1021/acscatal.3c00874.
[11] K. Chorozian, A. Karnaouri, T. Tryfona, N.G. Kondyli, A. Karantonis, E. Topakas, Characterization of a novel AA16 lytic polysaccharide monooxygenase from *Thermothelomyces thermophilus* and comparison of biochemical properties with an LPMO from AA9 family, Carbohydrate Polymers 342 (2024) 122387. https://doi.org/10.1016/j.carbpol.2024.122387.
[12] H.M. Nguyen, L.Q. Le, L. Sella, L.M. Broadbent, R.M. Bill, V.V. Vu, Heterologous expression and characterization of a *Mo*AA16 polysaccharide monooxygenase from the rice blast fungus *Magnaporthe oryzae*, Electronic Journal of Biotechnology 66 (2023) 1–16. https://doi.org/10.1016/j.ejbt.2023.06.002.
[13] G. Jagadeeswaran, L. Veale, A.J. Mort, Do Lytic Polysaccharide Monooxygenases Aid in Plant Pathogenesis and Herbivory?, Trends in Plant Science 26 (2021) 142–155. https://doi.org/10.1016/j.tplants.2020.09.013.
[14] L.B. Brenelli, G.F. Persinoti, J.P.L.F. Cairo, M.V. Liberato, T.A. Gonçalves, I.V.R. Otero, P.H. Mainardi, C. Felby, L.D. Sette, F.M. Squina, Novel redox-active enzymes for ligninolytic applications revealed from multiomics analyses of Peniophora sp . CBMAI 1063, a laccase hyper-producer strain, Scientific Reports 9 (2019) 1–15. https://doi.org/10.1038/s41598-019-53608-1.
[15] F. Teufel, J.J. Almagro Armenteros, A.R. Johansen, M.H. Gíslason, S.I. Pihl, K.D. Tsirigos, O. Winther, S. Brunak, G. von Heijne, H. Nielsen, SignalP 6.0 predicts all five types of signal peptides using protein language models, Nat Biotechnol 40 (2022) 1023–1025. https://doi.org/10.1038/s41587-021-01156-3.
[16] J.J. Almagro Armenteros, C.K. Sønderby, S.K. Sønderby, H. Nielsen, O. Winther, DeepLoc: prediction of protein subcellular localization using deep learning, Bioinformatics 33 (2017) 3387–3395. https://doi.org/10.1093/bioinformatics/btx431.
[17] I. Letunic, T. Doerks, P. Bork, SMART 6: recent updates and new developments., Nucleic Acids Research 37 (2009) D229-32. https://doi.org/10.1093/nar/gkn808.
[18] R. Zallot, N. Oberg, J.A. Gerlt, The EFI Web Resource for Genomic Enzymology Tools: Leveraging Protein, Genome, and Metagenome Databases to Discover Novel Enzymes and Metabolic Pathways, Biochemistry 58 (2019) 4169–4182. https://doi.org/10.1021/acs.biochem.9b00735.
[19] P. Di Tommaso, S. Moretti, I. Xenarios, M. Orobitg, A. Montanyola, J.-M. Chang, J.-F. Taly, C. Notredame, T-Coffee: a web server for the multiple sequence alignment of protein and RNA sequences using structural information and homology extension, Nucleic Acids Research 39 (2011) W13–W17. https://doi.org/10.1093/nar/gkr245.

[20] A.M. Waterhouse, J.B. Procter, D.M.A. Martin, M. Clamp, G.J. Barton, Jalview Version 2—a multiple sequence alignment editor and analysis workbench, Bioinformatics 25 (2009) 1189–1191. https://doi.org/10.1093/bioinformatics/btp033.
[21] F. Lemoine, D. Correia, V. Lefort, O. Doppelt-Azeroual, F. Mareuil, S. Cohen-Boulakia, O. Gascuel, NGPhylogeny.fr: new generation phylogenetic services for non-specialists, Nucleic Acids Research 47 (2019) W260–W265. https://doi.org/10.1093/nar/gkz303.
[22] I. Letunic, P. Bork, Interactive tree of life (iTOL) v3: an online tool for the display and annotation of phylogenetic and other trees, Nucleic Acids Res 44 (2016) W242–W245. https://doi.org/10.1093/nar/gkw290.
[23] M. Mirdita, K. Schütze, Y. Moriwaki, L. Heo, S. Ovchinnikov, M. Steinegger, ColabFold: making protein folding accessible to all, Nat Methods 19 (2022) 679–682. https://doi.org/10.1038/s41592-022-01488-1.
[24] J. Jumper, R. Evans, A. Pritzel, T. Green, M. Figurnov, O. Ronneberger, K. Tunyasuvunakool, R. Bates, A. Žídek, A. Potapenko, A. Bridgland, C. Meyer, S.A.A. Kohl, A.J. Ballard, A. Cowie, B. Romera-Paredes, S. Nikolov, R. Jain, J. Adler, T. Back, S. Petersen, D. Reiman, E. Clancy, M. Zielinski, M. Steinegger, M. Pacholska, T. Berghammer, S. Bodenstein, D. Silver, O. Vinyals, A.W. Senior, K. Kavukcuoglu, P. Kohli, D. Hassabis, Highly accurate protein structure prediction with AlphaFold, Nature 596 (2021) 583–589. https://doi.org/10.1038/s41586-021-03819-2.
[25] J. Yang, R. Yan, A. Roy, D. Xu, J. Poisson, Y. Zhang, The I-TASSER Suite: protein structure and function prediction, Nat. Methods 12 (2015) 7–8. https://doi.org/10.1038/nmeth.3213.
[26] G. Studer, C. Rempfer, A.M. Waterhouse, R. Gumienny, J. Haas, T. Schwede, QMEANDisCo—distance constraints applied on model quality estimation, Bioinformatics 36 (2020) 1765–1771. https://doi.org/10.1093/bioinformatics/btz828.
[27] Schrödinger, LLC, The PyMOL Molecular Graphics System, Version 1.8, (2015).
[28] N.A. Baker, D. Sept, S. Joseph, M.J. Holst, J.A. McCammon, Electrostatics of nanosystems: Application to microtubules and the ribosome, Proceedings of the National Academy of Sciences 98 (2001) 10037–10041. https://doi.org/10.1073/pnas.181342398.
[29] J.P.L. Franco Cairo, D.V. Almeida, A. Damasio, W. Garcia, F.M. Squina, The periplasmic expression and purification of AA15 lytic polysaccharide monooxygenases from insect species in *Escherichia coli*, Protein Expression and Purification 190 (2022) 105994. https://doi.org/10.1016/j.pep.2021.105994.
[30] J.P.L. Franco Cairo, D. Cannella, L.C. Oliveira, T.A. Gonçalves, M.V. Rubio, C.R.F. Terrasan, R. Tramontina, L.S. Mofatto, M.F. Carazzolle, W. Garcia, C. Felby, A. Damasio, P.H. Walton, F. Squina, On the roles of AA15 lytic polysaccharide monooxygenases derived from the termite Coptotermes gestroi, Journal of Inorganic Biochemistry 216 (2021) 111316. https://doi.org/10.1016/j.jinorgbio.2020.111316.
[31] M.-C. Lo, A. Aulabaugh, G. Jin, R. Cowling, J. Bard, M. Malamas, G. Ellestad, Evaluation of fluorescence-based thermal shift assays for hit identification in drug discovery, Anal. Biochem. 332 (2004) 153–159. https://doi.org/10.1016/j.ab.2004.04.031.
[32] P.S. Bond, (2017). http://paulsbond.co.uk/jtsa.
[33] M.N. Schulz, J. Landström, R.E. Hubbard, MTSA—A Matlab program to fit thermal shift data, Analytical Biochemistry 433 (2013) 43–47. https://doi.org/10.1016/j.ab.2012.10.020.
[34] D. Corrêa, C. Ramos, The use of circular dichroism spectroscopy to study protein folding, form and function, African J Biochem Res 3 (2009) 164–173. https://doi.org/not available.
[35] L.C. de Oliveira, V.M. da Silva, F. Colussi, A.D. Cabral, M. de O. Neto, F.M. Squina, W. Garcia, Conformational Changes in a Hyperthermostable Glycoside Hydrolase: Enzymatic Activity Is a Consequence of the Loop Dynamics and Protonation Balance, PLOS ONE 10 (2015) e0118225. https://doi.org/10.1371/journal.pone.0118225.

[36] M. Wasilewska, Z. Adamczyk, B. Jachimska, Structure of Fibrinogen in Electrolyte Solutions Derived from Dynamic Light Scattering (DLS) and Viscosity Measurements, Langmuir 25 (2009) 3698–3704. https://doi.org/10.1021/la803662a.
[37] S. Stoll, A. Schweiger, EasySpin, a comprehensive software package for spectral simulation and analysis in EPR, Journal of Magnetic Resonance 178 (2006) 42–55. https://doi.org/10.1016/j.jmr.2005.08.013.
[38] R. Kittl, D. Kracher, D. Burgstaller, D. Haltrich, R. Ludwig, Production of four Neurospora crassa lytic polysaccharide monooxygenases in Pichia pastoris monitored by a fluorimetric assay, Biotechnology for Biofuels 5 (2012) 79. https://doi.org/10.1186/1754-6834-5-79.
[39] E. Breslmayr, M. Hanžek, A. Hanrahan, C. Leitner, R. Kittl, B. Šantek, C. Oostenbrink, R. Ludwig, A fast and sensitive activity assay for lytic polysaccharide monooxygenase, Biotechnol Biofuels 11 (2018) 79. https://doi.org/10.1186/s13068-018-1063-6.
[40] Z. Forsberg, B. Bissaro, J. Gullesen, B. Dalhus, G. Vaaje-Kolstad, V.G.H. Eijsink, Structural determinants of bacterial lytic polysaccharide monooxygenase functionality, Journal of Biological Chemistry 293 (2018) 1397–1412. https://doi.org/10.1074/jbc.M117.817130.
[41] K.C. Tamburrini, S. Kodama, S. Grisel, M. Haon, T. Nishiuchi, B. Bissaro, Y. Kubo, S. Longhi, J.-G. Berrin, The disordered C-terminal tail of fungal LPMOs from phytopathogens mediates protein dimerization and impacts plant penetration, Proc Natl Acad Sci U S A 121 (2024) e2319998121. https://doi.org/10.1073/pnas.2319998121.
[42] T.J. Simmons, K.E.H. Frandsen, L. Ciano, T. Tryfona, N. Lenfant, J.C. Poulsen, L.F.L. Wilson, T. Tandrup, M. Tovborg, K. Schnorr, K.S. Johansen, B. Henrissat, P.H. Walton, L.L. Leggio, P. Dupree, Structural and electronic determinants of lytic polysaccharide monooxygenase reactivity on polysaccharide substrates, Nature Communications 8 (2017) 1064. https://doi.org/10.1038/s41467-017-01247-3.
[43] K.E.H. Frandsen, T.J. Simmons, P. Dupree, J.-C.N. Poulsen, G.R. Hemsworth, L. Ciano, E.M. Johnston, M. Tovborg, K.S. Johansen, P. von Freiesleben, L. Marmuse, S. Fort, S. Cottaz, H. Driguez, B. Henrissat, N. Lenfant, F. Tuna, A. Baldansuren, G.J. Davies, L. Lo Leggio, P.H. Walton, The molecular basis of polysaccharide cleavage by lytic polysaccharide monooxygenases, Nat Chem Biol 12 (2016) 298–303. https://doi.org/10.1038/nchembio.2029.
[44] Claire.A. Fowler, F. Sabbadin, L. Ciano, G.R. Hemsworth, L. Elias, N. Bruce, S. McQueen-Mason, G.J. Davies, P.H. Walton, Discovery, activity and characterisation of an AA10 lytic polysaccharide oxygenase from the shipworm symbiont Teredinibacter turnerae, Biotechnology for Biofuels 12 (2019) 232. https://doi.org/10.1186/s13068-019-1573-x.
[45] F. Sabbadin, G.R. Hemsworth, L. Ciano, B. Henrissat, P. Dupree, T. Tryfona, R.D.S. Marques, S.T. Sweeney, K. Besser, L. Elias, G. Pesante, Y. Li, A.A. Dowle, R. Bates, L.D. Gomez, R. Simister, G.J. Davies, P.H. Walton, N.C. Bruce, S.J. McQueen-Mason, An ancient family of lytic polysaccharide monooxygenases with roles in arthropod development and biomass digestion, Nat Commun 9 (2018) 756. https://doi.org/10.1038/s41467-018-03142-x.
[46] D. Kracher, M. Andlar, P.G. Furtmüller, R. Ludwig, Active-site copper reduction promotes substrate binding of fungal lytic polysaccharide monooxygenase and reduces stability, Journal of Biological Chemistry 293 (2018) 1676–1687. https://doi.org/10.1074/jbc.RA117.000109.
[47] M.A.S. Kadowaki, A. Várnai, J.-K. Jameson, A.E. T. Leite, A.J. Costa-Filho, P.S. Kumagai, R.A. Prade, I. Polikarpov, V.G.H. Eijsink, Functional characterization of a lytic polysaccharide monooxygenase from the thermophilic fungus Myceliophthora

thermophila, PLoS One 13 (2018) e0202148. https://doi.org/10.1371/journal.pone.0202148.
[48] L. Ciano, G.J. Davies, W.B. Tolman, P.H. Walton, Bracing copper for the catalytic oxidation of C–H bonds, Nature Catalysis 1 (2018) 571. https://doi.org/10.1038/s41929-018-0110-9.
[49] V.G.H. Eijsink, D. Petrovic, Z. Forsberg, S. Mekasha, Å.K. Røhr, A. Várnai, B. Bissaro, G. Vaaje-Kolstad, On the functional characterization of lytic polysaccharide monooxygenases (LPMOs), Biotechnology for Biofuels 12 (2019) 58. https://doi.org/10.1186/s13068-019-1392-0.
[50] C.R.F. Terrasan, M.V. Rubio, J.A. Gerhardt, J.P.F. Cairo, F.J. Contesini, M.P. Zubieta, F.L. de Figueiredo, F.L. Valadares, T.L.R. Corrêa, M.T. Murakami, T.T. Franco, G.J. Davies, P.H. Walton, A. Damasio, Deletion of AA9 Lytic Polysaccharide Monooxygenases Impacts A. nidulans Secretome and Growth on Lignocellulose, Microbiology Spectrum 10 (2022) e02125-21. https://doi.org/10.1128/spectrum.02125-21.
[51] G. Vaaje-Kolstad, B. Westereng, S.J. Horn, Z. Liu, H. Zhai, M. Sorlie, V.G.H. Eijsink, An Oxidative Enzyme Boosting the Enzymatic Conversion of Recalcitrant Polysaccharides, Science 330 (2010) 219–222. https://doi.org/10.1126/science.1192231.
[52] P.H. Walton, G.J. Davies, On the catalytic mechanisms of lytic polysaccharide monooxygenases, Current Opinion in Chemical Biology 31 (2016) 195–207. https://doi.org/10.1016/j.cbpa.2016.04.001.
[53] T.L.R. Corrêa, A.T. Júnior, L.D. Wolf, M.S. Buckeridge, L.V. dos Santos, M.T. Murakami, An actinobacteria lytic polysaccharide monooxygenase acts on both cellulose and xylan to boost biomass saccharification, Biotechnology for Biofuels 12 (2019) 117. https://doi.org/10.1186/s13068-019-1449-0.
[54] D. Floudas, M. Binder, R. Riley, K. Barry, R.A. Blanchette, B. Henrissat, A.T. Martinez, R. Otillar, J.W. Spatafora, J.S. Yadav, A. Aerts, I. Benoit, A. Boyd, A. Carlson, A. Copeland, P.M. Coutinho, R.P. de Vries, P. Ferreira, K. Findley, B. Foster, J. Gaskell, D. Glotzer, P. Gorecki, J. Heitman, C. Hesse, C. Hori, K. Igarashi, J.A. Jurgens, N. Kallen, P. Kersten, A. Kohler, U. Kues, T.K.A. Kumar, A. Kuo, K. LaButti, L.F. Larrondo, E. Lindquist, A. Ling, V. Lombard, S. Lucas, T. Lundell, R. Martin, D.J. McLaughlin, I. Morgenstern, E. Morin, C. Murat, L.G. Nagy, M. Nolan, R.A. Ohm, A. Patyshakuliyeva, A. Rokas, F.J. Ruiz-Duenas, G. Sabat, A. Salamov, M. Samejima, J. Schmutz, J.C. Slot, F. St. John, J. Stenlid, H. Sun, S. Sun, K. Syed, A. Tsang, A. Wiebenga, D. Young, A. Pisabarro, D.C. Eastwood, F. Martin, D. Cullen, I.V. Grigoriev, D.S. Hibbett, The Paleozoic Origin of Enzymatic Lignin Decomposition Reconstructed from 31 Fungal Genomes, Science 336 (2012) 1715–1719. https://doi.org/10.1126/science.1221748.